Asian Journal of Chemistry; Vol. 38, No. 6 (2026), 1589-1598
ASIAN JOURNAL OF CHEMISTRY
https://doi.org/10.14233/ajchem.2026.35930

Catalytic Functionalities of Palladium Supported on Zirconia Catalysts for Reductive-Amination of Phenol to Aniline

D. NARESH[1,2,*], B. VISWANADHAM[1,3,*], G. VIDYA SAGAR[1,2] and K.V.R. CHARY[1]

[1]Catalysis Division, Indian Institute of Chemical Technology, Hyderabad-500007, India
[2]SABIC Research & Technology Pvt. Ltd., Plot No. 81 to 85, Chikkadunnasandra, Sarjapura, Bangalore-562125, India
[3]Department of Chemistry, GMR Institute of Technology (GMRIT)-Deemed to be University, Rajam-532127, India

*Corresponding authors: E-mail: nareshdhachapally@gmail.com; viswanadham.b@gmrit.edu.in

Received: 10 March 2026 *Accepted*: 15 May 2026 *Published online*: 31 May 2026 AJC-22386

A series of active palladium species supported on zirconia, with varying Pd loadings (0.5-6 wt.%), were synthesised using the impregnation method and characterised through XRD, surface area and pore analysis, UV-DRS, XPS, H_2-TPR, CO_2-TPD and CO chemisorption. XRD patterns indicated the formation of a crystalline PdO phase for Pd loadings exceeding 2 wt.%. Pore size distribution analysis showed a decrease in both pore volume and diameter as Pd content increased. Moreover, the intensity ratio of the Pd $3d_{5/2}$ and Zr $3d_{5/2}$ XPS peaks exhibited a strong correlation with Pd dispersion values derived from CO chemisorption. UV-DRS and TPR analyses revealed the presence of two distinct palladium species on the ZrO_2 support, including highly dispersed PdO species reduced at lower temperatures and bulk PdO species reduced at comparatively higher temperatures. The basicity of the catalysts increased with Pd loading, followed by a reduction at higher loadings. The findings indicate that the number of exposed surface Pd sites increases with increasing Pd loading, reaches a maximum at 2 wt.% Pd, and remains nearly constant at higher loadings. The catalytic activity for the vapour-phase reductive amination of phenol to aniline increased with Pd loading up to 2 wt.% and decreased at higher loadings, consistent with the observed trends in active Pd sites and surface basicity. The higher turnover frequency (TOF) for smaller Pd particles decreases with increasing particle size up to 3 nm and remains nearly constant for larger particles. The strong dependence of catalytic activity on Pd crystallite size confirms that the reductive amination of phenol proceeds as a structure-sensitive reaction.

Keywords: Pd/ZrO_2 catalysts, Dispersion, Reductive amination, Phenol.

INTRODUCTION

Heterogeneous catalysts that utilize noble metals are vital instruments in the chemical industry, particularly for processes such as hydrogenation. Among these, catalysts supported by palladium have attracted considerable attention due to their remarkable performance at relatively low temperatures and pressures [1-3]. Extensive investigations have been conducted on these catalysts due to their exceptional activity and applicability in catalytic processes. The efficacy of these palladium supported catalysts is largely dependent on the degree to which the active phase is distributed across the support material. This distribution is not arbitrary; it is affected by numerous factors, including the type of oxide that supports the palladium, the presence of any promoters or additives, the amount of loading and the specific preparation method employed. The surface condition of the active palladium component, whether it remains finely dispersed or aggregates into larger crystallites, is significantly influenced by the catalyst's fabrication process, the acidity and basicity of the support and the quantity of palladium introduced [4]. Grasping the characteristics of this active phase and its interaction with the support is essential. Such understanding help researchers and scientists in optimizing catalyst design, thereby ensuring enhanced efficiency and stability during reactions. Every aspect, from preparation methods to the properties of the supports, contributes to shaping the behaviour of the catalysts, an intricate interplay that scientists continue to explore with great interest. Consequently, there is a steadily increasing interest among catalytic researchers in this field to discover new supports that can address some of the critical issues (such as performance and deactivation) and also to prolong the lifespan of catalyst.

Zirconia is an attractive catalyst support due to its high thermal stability, chemical inertness and the presence of both

acidic and basic surface functionalities. In addition, its strong metal-support interaction and excellent mechanical stability enable the formation of stable and well-dispersed active phases [5]. Zirconia-supported catalysts have been widely employed in various catalytic reactions, including methane oxidation over Pd–Pt [6], alcohol upgrading over Cu [7], CO_2 methanation over Ni [8], hydrogen production over Co–Mn [9], NO reduction over vanadium catalysts [10], hydrogenation and dehydrogenation over Fe catalysts [11,12] and methanol oxidation over chromium oxide [13].

Among these systems, Pd/ZrO_2 catalysts have shown superior catalytic performance compared to Pd supported on conventional oxides such as Al_2O_3, SiO_2 and TiO_2 for methanol synthesis from CO hydrogenation [14]. Iwasa *et al*. [15] also reported that Pd/ZrO_2 exhibits excellent activity for methanol decomposition, while Okumura *et al*. [16] demonstrated its high activity in toluene combustion. Despite these promising catalytic properties, limited studies have focused on the interaction between palladium active sites and the zirconia support in Pd/ZrO_2 catalysts for the conversion of phenol to amine derivatives.

Aniline and its derivatives have attracted significant attention due to their wide range of industrial applications [17]. The presence of an amino group makes aniline an important intermediate in the production of dyes, antioxidants, pharmaceuticals, agrochemicals and rubber-processing chemicals. It is also a key precursor for isocyanate synthesis, which is essential for polyurethane production used in plastics, insulation materials and fibres. Commercially, aniline is mainly produced from benzene through either catalytic hydrogenation of nitrobenzene or ammonolysis of chlorobenzene under severe operating conditions. Since phenol is an inexpensive feedstock and an important industrial pollutant generated from petrochemical and polymer industries [18,19], its conversion into value-added chemicals is highly desirable. Among the available methods, the reductive amination of phenol with ammonia and hydrogen to produce aniline in a single step has emerged as an attractive and economically promising route for industrial application [20-23]. However, the process still faces challenges such as the requirement for elevated temperatures and pressures along with limited product yields.

This study presents the synthesis of aniline from phenol utilizing palladium supported on zirconia catalysts. Various palladium–zirconia catalysts with different Pd loadings were synthesised and thoroughly characterised through techniques including X-ray diffraction (XRD), UV-visible diffuse reflectance spectroscopy (UV-DRS), X-ray photoelectron spectroscopy (XPS), temperature-programmed reduction (TPR) and CO_2 temperature-programmed desorption (CO_2-TPD). The palladium dispersion, metal surface area and crystallite size were further assessed using the CO chemisorption method. The catalytic performance of these catalysts was tested in the vapour-phase reductive amination of phenol to aniline. The main aim of this research is to explore the correlation between Pd dispersion on zirconia and the catalytic performance in phenol reductive amination. Furthermore, the activity of Pd/ZrO_2 catalysts is compared with that of Pd supported on alternative materials, such as magnesia and silica, to evaluate the influence of the support on catalytic performance.

EXPERIMENTAL

Catalyst synthesis

Preparation of support: The zirconia support was prepared by dissolving zirconyl nitrate hydrate ($ZrO(NO_3)_2{\cdot}xH_2O$, Aldrich) in deionised water to obtain a 0.5 M solution. A 10% aqueous NH_3 solution was added dropwise under vigorous stirring until the pH reached 9. The suspension was further stirred for 30 min to ensure complete precipitation of Zr^{4+} ions. The resulting white $Zr(OH)_4$ precipitate was separated by vacuum filtration and washed repeatedly with deionised water until the filtrate attained neutral pH. The obtained $Zr(OH)_4$ cake was dried at 120 ºC for 16 h and subsequently pulverised into a fine powder. Calcination was carried out in a muffle furnace under a continuous air flow of 100 mL/min using a stepwise heating programme. The sample was heated to 150 ºC at a rate of 0.5 ºC/min and held for 30 min, followed by heating to 300 ºC at the same ramp rate and holding for another 30 min. Finally, the temperature was increased to 500 ºC at 0.5 ºC/min and maintained for 5 h.

Preparation of catalyst: The palladium-supported zirconia catalysts were prepared by the wet impregnation method. A series of Pd/ZrO_2 catalysts containing 0.5-6 wt.% Pd were synthesised. The required amount of $PdCl_2$ was dissolved in 0.1 M aqueous HCl at 323 K under vigorous stirring to form $[PdCl_4]^{2-}$ species, which was subsequently used as precursor solution for impregnation. After complete dissolution, deionised water was added to obtain a total solution volume approximately 15% higher than the pore volume of the zirconia support. The pore volume of zirconia was determined by the incipient wetness method using deionised water and zirconia previously dried at 120 ºC for 12 h. The prepared Pd precursor solution was slowly added to the dried zirconia support under continuous mixing to ensure uniform impregnation. Excess water was removed by evaporation at 80 ºC with constant stirring. The impregnated material was equilibrated at room temperature for 2 h and subsequently dried at 120 ºC for 12 h. The dried catalyst was calcined in a muffle furnace under a continuous air flow of 100 mL/min using a stepwise heating programme. The temperature was raised to 150 ºC at a heating rate of 0.5 ºC/min and maintained for 30 min, followed by heating to 300 ºC at the same rate and holding for another 30 min. Finally, the sample was heated to 500 ºC at 0.5 ºC/min and maintained for 5 h to obtain the active Pd/ZrO_2 catalysts. Although most chlorine species are expected to be removed during calcination, the presence of trace residual chlorine cannot be completely ruled out. Other supported catalysts were prepared following a similar procedure using commercial supports such as γ-Al_2O_3 (surface area = 175 m^2/g), SiO_2 (surface area = 370 m^2/g) and activated carbon (surface area = 1414 m^2/g).

Catalysts characterisation: Powder X-ray diffraction patterns were recorded on a Rigaku Miniflex diffractometer using nickel-filtered Cu*K*α radiation (λ = 1.5406 Å) at 40 kV and 30 mA, with a secondary graphite monochromator. Data were collected in the 2θ range of 2-75º with a step size of 0.045º and a counting time of 0.5 s per step. However, the data was presented from 20-75º of 2θ range only, since no significant reflections appeared below 20º. Phase identification was performed using the JCPDS database.

The specific surface areas of the zirconia support and Pd/ZrO_2 catalysts were determined from N_2 adsorption–desorption isotherms at 77 K using the multipoint BET (Brunauer–Emmett–Teller) method on a Quantachrome Autosorb-1 instrument. Prior to analysis, the samples were outgassed at 473 K for 5 h. A cross-sectional area of 0.164 nm^2 per N_2 molecule was used in the BET calculations. Pore size distribution (PSD) was determined from the desorption branch of the N_2 isotherm using the Barrett–Joyner–Halenda (BJH) method.

CO chemisorption measurements were performed using a dynamic pulse method on a Micromeritics AutoChem 2910 instrument equipped with a thermal conductivity detector (TCD). Approximately 100 mg of the sample was first reduced in a hydrogen flow (50 mL/min) at 500 ºC for 2 h, followed by flushing with helium (50 mL/min) for 1 h at the same temperature. After cooling to 303 K, pulses of CO (9.96% CO in He) were injected from a calibrated online sampling valve into the helium stream flowing over the reduced sample. Adsorption was considered complete when three consecutive pulses exhibited identical peak areas. The total CO uptake was quantified using GRAMS/32 software to calculate the palladium dispersion and metal surface area.

Palladium dispersion (D_{Pd}), defined as the ratio of surface-exposed Pd atoms to the total Pd atoms present, was determined from irreversible CO chemisorption obtained by pulse CO analysis. A CO/Pd surface stoichiometry of 1 was assumed for the calculations [21,24-26]. Although bridge-bonded CO adsorption may occur at higher Pd loadings, only single-site linear adsorption was considered for dispersion estimation in this study. Pd dispersion was calculated using $D_{Pd} = N_s/N_t$, where Ns represents the total irreversibly chemisorbed CO molecules (CO_{irr}) and N_t denotes the total number of Pd atoms per gram of catalyst. The catalyst metal surface area (S_{cat}), Pd metal surface area (S_{Pd}) and mean particle size (d) were calculated using eqns. 1-3:

$$S_{cat}\ (m^2/g_{cat}) = Mol_{CO} \times N_A \times SF/A \times 10^3 \quad (1)$$

$$S_{Pd}\ (m^2/g_{Pd}) = S_{cat.}\ 100/W_{Pd} \quad (2)$$

$$d\ (nm) = 6000/S_{Pd} \times \rho \quad (3)$$

$$\text{Pd density} = Mol_{CO} \times N_A/\text{zirconia surface area}\ (m^2/g) \quad (4)$$

where Mol_{CO}, N_A, SF, A, W_{Pd} and ρ represent the molecules of CO that are experimentally consumed per unit mass of catalyst (Mol_{CO} = μmolCO/g_{cat}), Avogadro's number (NA = 6.023×10^{-23} mol^{-1}), the stoichiometric factor (SF = 1), the number of surface atoms per square meter of the polycrystalline Pd surface (A = 1.47×10^{-19}), the percentage of Pd (W_{Pd} = wt.%) and the density of palladium (ρ = 12.02 g cm^{-3}).

UV-DRS spectra were recorded at room temperature in air using a GBC UV-Vis Cintra 10e spectrometer equipped with a diffuse reflectance accessory. Measurements were performed over the wavelength range of 200-800 nm using pure ZrO_2 as the reference material. The Kubelka-Munk function F(R) was plotted against wavelength to evaluate the optical properties of the samples. The XPS spectra of the catalysts were recorded on a Kratos Axis 165 spectrometer using Mg*K*α radiation (hν = 1253.6 eV) operated at 75 W. The Pd 3*d* and Zr 3*d* core-level spectra were collected and binding energies were referenced to the C 1*s* peak at 284.6 eV with an accuracy of ±0.2 eV. All measurements were carried out under ultra high vacuum conditions with a background pressure below 10^{-10} bar.

TPR measurements were performed on a Micromeritics AutoChem 2910 instrument to investigate the reducibility and dispersion of palladium species. Approximately 100 mg of dried sample was placed in a U-shaped quartz reactor supported by quartz wool. Prior to reduction, the catalyst was pretreated in helium flow (50 mL/min) at 200 ºC for 2 h to remove surface contaminants. After cooling to room temperature under helium, TPR analysis was carried out using a 5% H_2-Ar mixture (50 mL/min) with a heating rate of 10 K/min from ambient temperature to 550 ºC. Hydrogen consumption was monitored using a thermal conductivity detector (TCD) and T_{max} values were determined using GRAMS/32 software.

CO_2-TPD experiments were conducted on a Micromeritics AutoChem 2910 instrument to evaluate the basic properties of the catalysts. Approximately 150 mg of sample was reduced in hydrogen flow (50 mL/min) at 500 ºC for 2 h followed by helium purging at the same temperature for 1 h. The sample was then cooled to 30 ºC and saturated with 10% CO_2-He mixture (75 mL/min) for 1 h. Physisorbed CO_2 was removed by helium flushing (50 mL/min) at 105 ºC for 2 h. The TPD analysis was performed from room temperature to 1073 K at a heating rate of 10 K/min and the desorbed CO_2 was quantified using a TCD and GRAMS/32 software.

Catalytic reaction: The catalytic performance of the supported palladium catalysts was evaluated through the reductive amination of phenol to aniline in a down-flow fixed-bed Pyrex glass reactor operated at atmospheric pressure. The reactor had an internal diameter of 12 mm and was equipped with a 4 mm O.D. glass thermowell for monitoring the catalyst bed temperature. The reactor was placed inside an electrically heated split-type furnace. The catalyst powder was pelletized, crushed and sieved to obtain particle sizes in the range of 0.25-0.5 mm to ensure plug-flow behaviour. Approximately 0.5 g of catalyst was mixed with an equal volume of quartz grains and packed between quartz wool layers. Additional quartz grains of similar size were placed above the catalyst bed to act as a preheating zone. Prior to the reaction, the catalyst was reduced in hydrogen flow (50 mL/min) at 773 K for 2 h and subsequently cooled to the reaction temperature under hydrogen atmosphere.

The reaction feed consisted of phenol and cyclohexane in a weight ratio of 1:2 along with hydrogen and ammonia in a molar ratio of 1:5:5. The phenol–cyclohexane mixture was introduced at a flow rate of 4 mL/h using a calibrated motorized syringe pump. Catalytic reactions were carried out at 250 ºC under continuous-flow conditions and the system was maintained for 2 h prior to product collection to attain steady-state operation. The liquid products including aniline, cyclohexylamine and unreacted phenol were collected at the reactor outlet using a cold trap immersed in an ice bath. Product analysis was performed using a HP 6890 gas chromatograph equipped with a flame ionization detector (FID) and an HP-5 column. Product identification was further confirmed using a HP-5973 quadrupole GC-MS system.

The conversion of phenol along with product yield and selectivity were calculated using standard molar balance equations where n represents the number of moles of each component, i denotes the individual products and N corresponds to the carbon number of each component.

$$\text{Conversion of phenol (\%)} = \frac{n_{\text{Phenol,in}} - n_{\text{Phenol,out}}}{n_{\text{Phenol,in}}} \times 100$$

$$\text{Yield of product, i (\%)} = \frac{n_{\text{i,out}}}{n_{\text{Phenol,in}}} \times 100$$

$$\text{Selectivity of product, i (\%)} = \frac{n_{\text{i,out}}}{n_{\text{Phenol,in}} - n_{\text{Phenol,out}}} \times \frac{Z_i}{Z_{\text{Phenol}}} \times 100$$

To investigate the relationship between phenol reductive amination and palladium content, a correlation was established between palladium loading and TOF. Here, TOF is defined as the rate of reactant molecules converted per second per active Pd site. Turnover frequency (TOF) was calculated using the following expressions, where No of active Pd atoms is equal to total CO uptake in CO chemisorption method [21,27].

$$\text{Rate (mol s}^{-1}\text{g}_{\text{cat}}^{-1}\text{)} = \frac{\text{Phenol flow rate (mol/s)} \times \text{Fractional conversion of phenol}}{\text{Weight of the catalyst (g)}}$$

$$\text{Turnover frequency (TOF)} = \frac{\text{Rate}}{\text{Number of active Pd atoms}}$$

RESULTS AND DISCUSSION

XRD studies: The powder X-ray diffraction (XRD) analysis of the ZrO_2 support and various PdO/ZrO_2 catalyst profiles is shown in Fig. 1. Generally, ZrO_2 can be found in three crystallographic forms *viz*. monoclinic, tetragonal and cubic. The zirconia synthesised in this study demonstrates a mixed-phase structure that includes both monoclinic and tetragonal ZrO_2, as verified by the XRD pattern (Fig. 1). The XRD profile of ZrO_2 reveals distinct diffraction peaks at 2θ = 24.5º, 28.2º, 30.2º, 31.4º, 34.1º, 35.3º, 38.6º, 41.1º, 45.0º, 45.3º, 50.1º, 50.7º, 60.2º and 62.8º, which correspond to the respective *d*-spacings of 3.63, 3.16, 2.96, 2.85, 2.63, 2.54, 2.33, 2.20, 2.01, 2.00, 1.82, 1.80, 1.54 and 1.48 Å. The diffraction peaks identified at 2θ = 24.5º, 28.2º, 31.4º, 34.1º, 38.6º, 41.1º, 45.0º and 50.1º are associated with the monoclinic phase of ZrO_2 (JCPDS No. 37-1484), whereas the peaks at 30.2º, 35.3º, 45.3º, 50.7º, 60.2º and 62.8º are linked to the tetragonal ZrO_2 phase (JCPDS No. 80-2155). The XRD patterns for all palladium-supported catalysts did not reveal any detectable diffraction peaks that correspond to crystalline PdO. The characteristic peaks of PdO are observed at 2θ = 33.8º (d = 2.64 Å), which corresponds to the (101) plane with a relative intensity of 100%, along with two very weak reflections at approximately 2θ = 41.9º and 54.8º (JCPDS No. 46-1043). This absence may be attributed to the primary PdO peak at 2θ = 33.8º being obscured by the strong zirconia peak at 2θ = 34.1º. Nevertheless, the diffraction peak at 2θ = 34.1º significantly increased in intensity for the catalyst with 4 wt.% Pd loading compared to those with 2 wt.% Pd. The heightened intensity of the peak at 2θ = 34.1º may be ascribed to the presence of PdO crystallites.

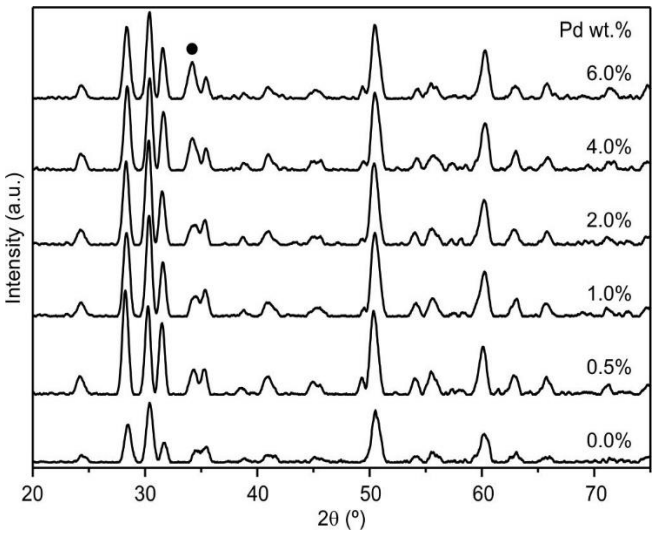

Fig. 1. X-ray diffraction patterns of pure ZrO_2 and various Pd/ZrO_2 catalysts (• is due to PdO)

The absence of PdO reflections at lower Pd loadings indicates that palladium species are highly dispersed on the ZrO_2 support or exist as very small nanoparticles below the XRD detection limit. Strong metal-support interactions may also inhibit the formation of bulk crystalline PdO, leading to highly dispersed or amorphous PdO species with crystallite sizes below 3 nm. Such high dispersion is beneficial for catalytic applications due to the increased availability of accessible active sites. No distinct reflections corresponding to mixed oxide phases between PdO and ZrO_2 were observed. However, overlapping diffraction peaks make the identification of bulk PdO crystallites difficult in Pd/ZrO_2 catalysts.

BET studies: The BET surface areas and pore properties of the catalysts are summarized in Table-1. The pure ZrO_2 support exhibited a surface area of 68 m²/g. A gradual decrease in surface area was observed with increasing Pd loading, likely due to pore occupation by Pd species. Nitrogen adsorption–desorption isotherms and pore size distribution profiles confirmed the mesoporous nature of the materials with pore diameters mainly distributed between 120-180 Å and a maximum around 150 Å. Both pore volume and average pore diameter decreased with increasing Pd loading due to partial pore filling and agglomeration of Pd species during calcination.

TABLE-1
BET SURFACE AREA, TOTAL PORE VOLUME AND AVERAGE PORE DIAMETER OF VARIOUS Pd/ZrO_2 CATALYSTS

Pd loading (wt.%)	BET surface area (m^2/g)	Total pore volume (mL/g)	Average pore diameter (Å)
ZrO_2	68	0.50	163
0.5	66	0.48	156
1.0	64	–	–
2.0	59	0.46	147
4.0	54	–	–
6.0	50	0.43	148

CO chemisorption data presented in Table-2 show that Pd dispersion decreased from 94% to 24% with increasing Pd loading, while Pd crystallite size increased correspondingly.

TABLE-2
Pd CONTENT, CO UPTAKE, DISPERSION, Pd METAL AREA AND Pd CRYSTALLITE SIZE OF VARIOUS Pd/ZrO_2 CATALYSTS

Pd loading (wt.)	Pd content (μmol/g_{cat})	CO uptake (μmol/g_{cat})	Dispersion (%)	Metal area (m^2/g_{pd})	Crystallite size (nm)
0.5	47.0	44.7	94	420	1.18
1.0	94.0	78.9	84	374	1.33
2.0	187.9	129.7	69	307	1.62
4.0	375.9	139.1	37	165	3.02
6.0	563.8	135.3	24	107	4.66

The high dispersion at lower Pd contents is attributed to strong interactions between Pd^{2+} and hydroxyl groups on the ZrO_2 surface. At higher loadings, Pd deposition on the external surface promotes agglomeration, resulting in lower dispersion and reduced metal surface area available for CO chemisorption.

UV-DRS studies: The UV-DRS spectra of Pd/ZrO_2 catalysts displayed absorption bands at 245 and 450 nm. The band at 245 nm is assigned to ligand-to-metal charge transfer involving highly dispersed Pd^{2+} species interacting with the ZrO_2 surface through Zr–O–Pd linkages [28]. The broad band at 450 nm corresponds to the *d–d* transition of bulk PdO species (Fig. 2). At lower Pd loadings, the absence of the 450 nm band indicates highly dispersed PdO species or extremely small PdO particles. The appearance and increasing intensity of the 450 nm band at and above 2 wt.% Pd indicate the formation and growth of bulk PdO crystallites. These results suggest the coexistence of two palladium species, namely highly dispersed PdO and bulk PdO, which is consistent with the CO chemisorption results.

XPS studies: XPS analysis was carried out to examine the oxidation states and surface composition of Pd/ZrO_2 catalysts. The Zr $3d_{5/2}$ binding energy remained nearly constant at approximately 182 eV irrespective of Pd loading. The Pd $3d_{5/2}$ and Pd $3d_{3/2}$ binding energies were observed in the ranges of 337.0-337.5 eV and 342.4-342.8 eV, respectively (Table-3), which are higher than those of bulk PdO [29,30]. These higher binding energies indicate the presence of electron-deficient Pd^{2+} species arising from strong metal–support interaction (SMSI) between Pd and ZrO_2. The interaction is associated with Pd–O–Zr bonding at the interface rather than Pd–O–Pd bonding.

TABLE-3
BINDING ENERGIES (eV), FWHM AND XPS ATOMIC RATIO OF Pd $3d_{5/2}$ AND Zr $3d_{5/2}$ of VARIOUS Pd/ZrO_2 CATALYSTS

Pd loading (wt.%)	Binding energy of Zr $3d_{5/2}$ (FWHM)	Binding energy of Pd $3d_{5/2}$ (FWHM)	XPS intensity Pd 3d/Zr 3d
0.5	182.0 (2.0)	337.5 (2.2)	0.08
1.0	181.9 (2.1)	337.4 (2.3)	0.12
2.0	182.1 (1.9)	337.2 (2.2)	0.15
4.0	182.0 (1.9)	337.10 (2.1)	0.16
6.0	181.9 (2.0)	337.0 (2.2)	0.16

With increasing Pd loading, the Pd binding energies decreased up to 4 wt.% and remained nearly constant thereafter. This behaviour reflects weaker metal–support interaction and larger Pd particles at higher Pd contents. Similar particle-size-dependent binding energy shifts have been reported by

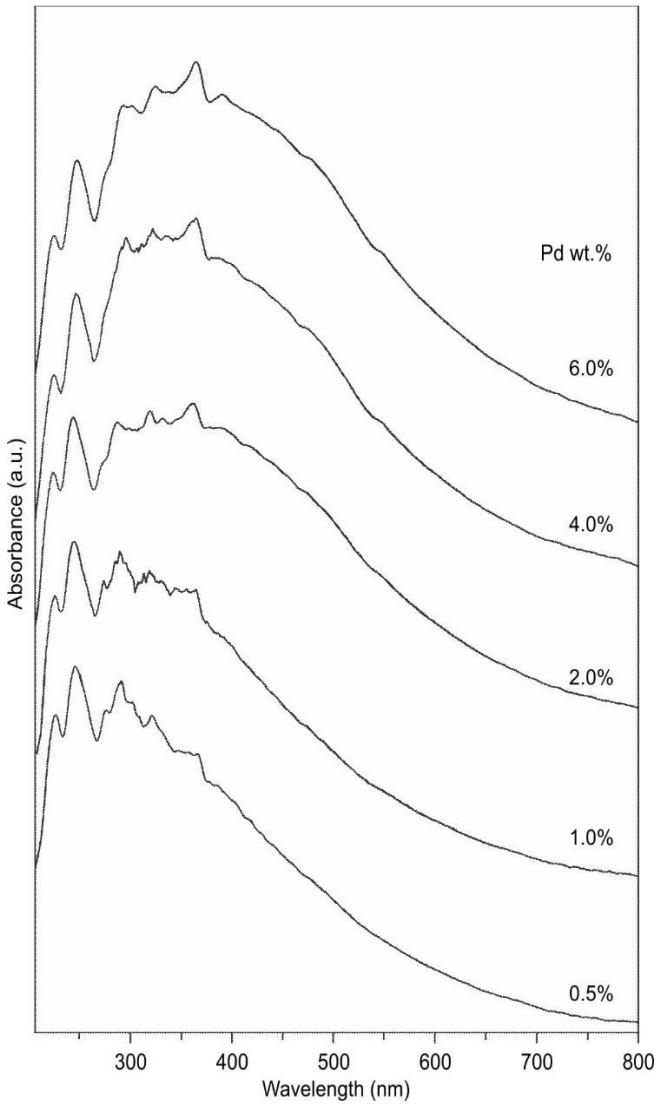

Fig. 2. UV-Vis diffuse reflectance spectra of various Pd/ZrO_2 catalysts

Voogt *et al.* [29], Takasu *et al.* [31], Fleisch [32] and Babu *et al.* [33]. The XPS peak intensity increased with Pd loading up to 2 wt.% and remained nearly unchanged at higher loadings, indicating that the number of exposed surface Pd sites reaches saturation beyond 2 wt.% due to the formation of larger PdO agglomerates (Fig. 3). The constant FWHM values also support the coexistence of highly dispersed Pd species and bulk PdO species. The Pd $3d_{5/2}$/Zr $3d_{5/2}$ intensity ratios further confirmed that the surface Pd concentration increases up to 2 wt.% Pd and remains nearly constant thereafter, which is in excellent agreement with the CO chemisorption results.

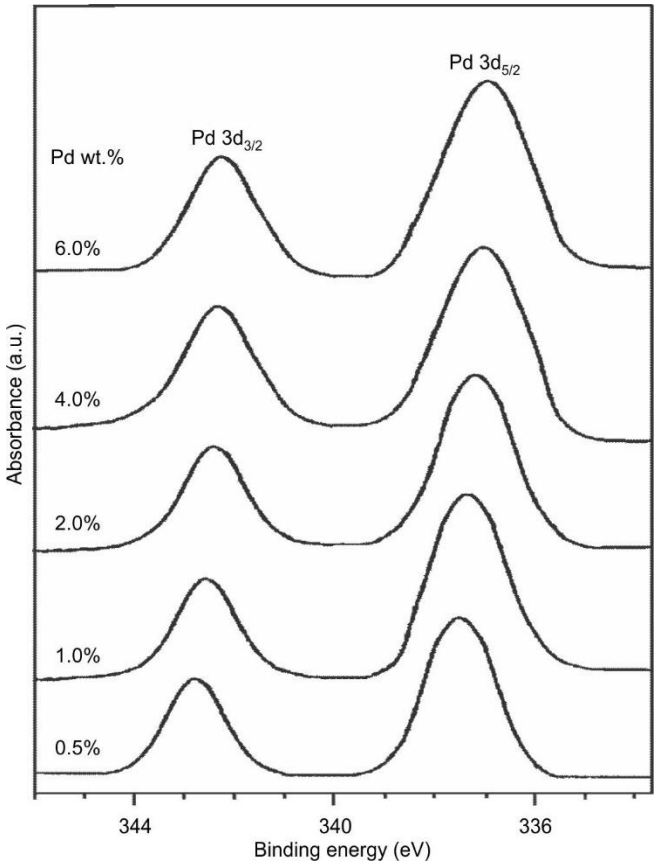

Fig. 3. Pd 3d XPS spectra of various Pd/ZrO_2 catalysts

Temperature programmed reduction (TPR): The TPR profiles for various palladium-supported ZrO_2 catalysts are illustrated in Fig. 4. The associated maximum reduction temperature (T_{max}) and the corresponding hydrogen consumption values are presented in Table-4. The TPR profiles display two distinct reduction peaks *viz.* one positive and the other negative. The positive peak is notably broad, commencing at 474 K and concluding at 673 K. The peak maximum (T_{max}) varies with different Pd loadings, shifting to lower temperatures from 602 K for a 0.5 wt.% Pd loading to 560 K for a 6 wt.% loading. This reduction peak is attributed to the conversion of Pd^{2+} or PdO to the metallic form of palladium. In the current catalyst system, the reduction temperature of PdO is significantly higher than that of bulk PdO reported in the literature. The shift of the reduction temperature towards higher values clearly indicates a strong interaction between Pd^{2+} ions and ZrO_2, which impedes the reduction of PdO, consistent with previous studies [34,35]. As the palladium content increases from 0.5 to 6 wt.%, the maximum reduction temperature (T_{max}) decreases from 602 K to 560 K, suggesting that at lower Pd loadings, the palladium ions exist in a highly dispersed state as smaller PdO particles, facilitating a strong metal-support interaction characterised by highly coordinated Pd species with the support or Zr-O-Pd bonds. This robust metal-support interaction or the presence of highly coordinated species leads to increased resistance to reduction to their metallic form [34-36]. Furthermore, the intensity of the positive peak increases with rising palladium loading up to 2 wt.% (Fig. 4) and subsequently decreases at higher Pd loadings. This clearly indicates that the population of dispersed Pd^{2+} ions increases

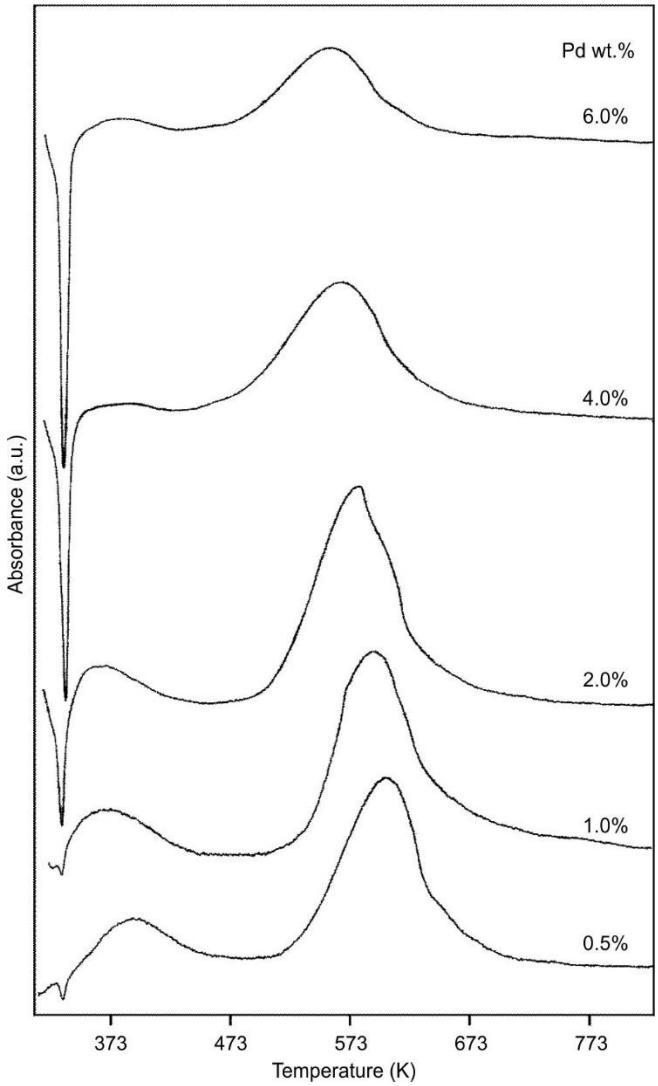

Fig. 4. Temperature programmed reduction profiles of various Pd/ZrO_2 catalysts

TABLE-4
TEMPERATURE PROGRAMMED REDUCTION OF H_2 RESULTS OF VARIOUS Pd/ZrO_2 CATALYSTS

Pd loading (wt.%)	T_{max}^1 (K) (negative)	H_2 consumption (μmol/g)	T_{max}^2 (K) (positive)	H_2 consumption (μmol/g)	Total H_2 consumption (negative peak + positive peak) (μmol/g)
0.5	–	–	602	59	59
1.0	–	–	588	82	82
2.0	331	21	574	165	186
4.0	334	71	568	189	260
6.0	334	119	560	183	302

and then decreases with further increases in Pd loadings. These findings suggest that the palladium dispersion increases with an increase in Pd loading up to 2 wt.% and decreases with further increases in palladium loading. The hydrogen consumption also follows a similar trend to that of the reduction.

A distinct fingerprint TPR pattern characterised by a negative peak observed in current Pd catalyst systems (Fig. 4). The TPR profiles of these catalysts reveal a significant negative peak beginning at 2 wt.% around 334 K, with intensity increasing as the Pd loading rises. This negative peak formation is linked to the decomposition and subsequent release of hydrogen from the β-PdHx phase [33,37,38]. Generally, in palladium catalysts, a portion of the Pd^{2+} ions undergo reduction at room temperature, after which the reduced Pd metal dissociates hydrogen, which is then absorbed onto the metal, resulting in the formation of an unstable β-Pd hydride phase. During this process, some hydrogen molecules are simultaneously dissociated on the Pd crystals that develop at higher loadings, contributing to the formation of the unstable β-Pd hydride phase. This phase subsequently releases molecular hydrogen when the temperature is raised to 334 K, leading to a pronounced negative peak. As the palladium loading on ZrO_2 continues to increase, the intensity of the negative peak also escalates due to the formation of larger Pd particles within the catalyst, which facilitates the development of additional β-PdHx phase, as depicted in Fig. 4. At elevated Pd loadings, the palladium crystallites occupy the external surface of the support, forming larger crystallites or agglomerates that are reduced at room temperature. With an increase in Pd loading, the consumption of the β-PdHx peak also intensifies due to the enlargement of particle size. However, the positive peak hydrogen uptake increases up to a specific loading and remains stable at higher loadings, which is attributed to the reduction of PdO occurring solely at room temperature (Table-4). These findings are in strong agreement with CO chemisorption and XPS results.

Correlation studies: A correlation between several critical properties and palladium loadings is depicted in Fig. 5. As shown in Fig. 5, the surface area of the Pd metal and the Pd density derived from CO uptake, the Pd/Zr surface composition ratio obtained from XPS spectra and the hydrogen consumption linked to the positive reduction of PdO (Pd–O–Zr species) measured through temperature-programmed reduction all rise with Pd loading up to 2 wt.%, after which they remain nearly unchanged at higher Pd loadings. The findings suggest that the active density of Pd surface increases with Pd loading up to 2 wt.% and stays almost constant at greater loadings; a similar pattern is noted for the catalyst's Pd surface area. The Pd/Zr surface composition ratio measured by XPS, which is restricted to examining the near-surface region, also increases with Pd loading up to 2 wt.% and remains nearly constant at higher Pd loadings. The hydrogen consumption related to the PdO reduction peak, which is attributed to highly dispersed or support-interacted Pd species, also rises with Pd loading up to 2 wt.% and exhibits no significant variation at higher loadings. In summary, the results indicate that the number of exposed surface Pd sites increases with Pd loading, reaches a plateau at 2 wt.% Pd and remains fundamentally constant at higher loadings.

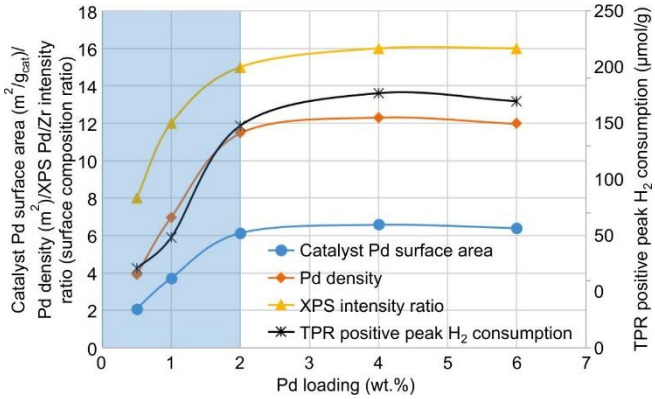

Fig 5. A correlation between Pd metal surface area, Pd density, XPS Pd/Zr surface composition ratio, TPR positive peak hydrogen consumption for various Pd/ZrO_2 catalysts

The assessments of basicity for Pd/ZrO_2 catalysts were performed using temperature programmed desorption (TPD) of CO_2, with the results illustrated in Fig. 6. The TPD technique for CO_2 is a commonly employed and effective method for assessing both the basicity and the basic strength of solid catalysts. The basicity of an oxide surface is generally linked to the electron-donating properties of the associated oxygen anions; therefore, a higher partial negative charge on the oxygen is indicative of increased basic strength. The total number of basic sites along with their density and strength distribution are shown in Table-5. As per the existing literature [21,25,39,40], the basic strength of the materials can be classified into three categories based on CO_2-TPD: weak (373-523 K), medium (523-653 K) (for instance, OH and O groups) and strong basic sites (623-873 K) (coordinatively unsaturated oxygen ions O^{2-} or Pd and Zr). As shown in Fig. 6, the TPD profiles display similar shapes across different palladium loadings. The peak observed around 430 K is likely linked to weak basic sites, which may correspond to lattice-bound -OH groups or surface hydroxyl groups. The peak located near 683 K is associated with the strong basic sites of coordinatively unsaturated oxygen ions (*e.g.* O^{2-}) and with the introduction of Pd, both weak and strong basic sites increased, although the increase in weak basic sites was more pronounced compared to strong basic sites. The formation of Pd^{2+}-O^{2-} acid-base pair junctions may account for the enhancement in basicity. The overall basicity increases with Pd loading up to 2 wt.%, but decreases at higher Pd concentrations. The basicity of the catalysts is predominantly affected by the Pd phase, as CO_2 uptake rises with increased Pd loading [21]. The reduction in basicity at higher loadings is attributed to

TABLE-5
TEMPERATURE PROGRAMMED DESORPTION OF CO_2 OF PURE ZrO_2 AND VARIOUS Pd/ZrO_2 CATALYSTS

Pd loading (wt.%)	CO_2 uptake (µmol/g)		Total basicity (µmol/g)
	Weak	Medium	
0.0	136	247	383
0.5	181	257	438
1.0	186	277	463
2.0	195	318	513
4.0	183	285	468
6.0	165	253	418

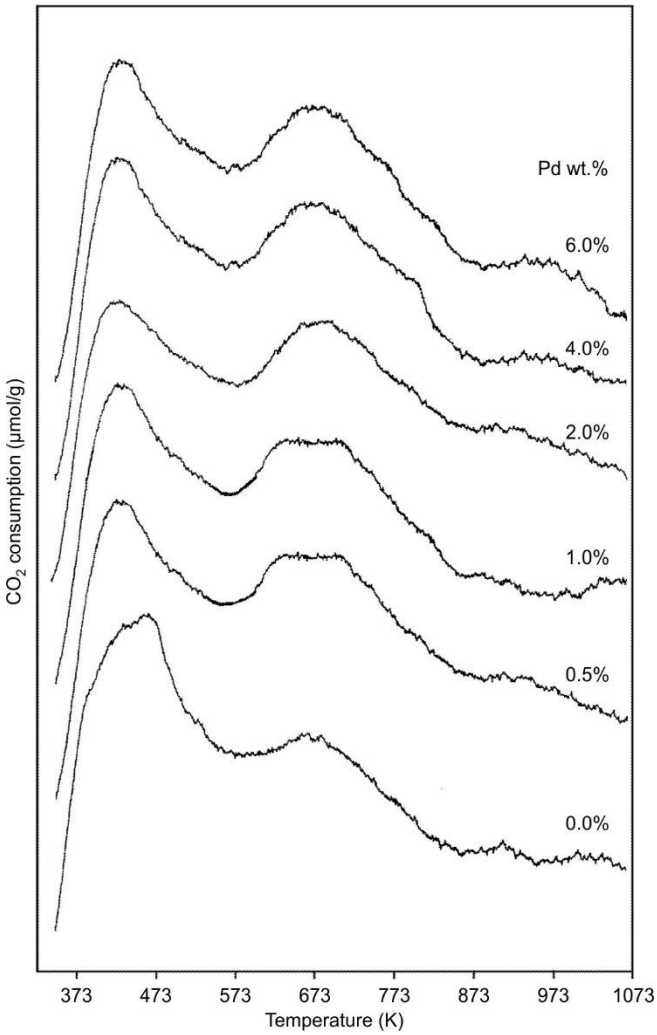

Fig. 6. Temperature programmed desorption of CO_2 of pure ZrO_2 support and various Pd/ZrO_2 catalysts

the development of Pd crystallites, indicating that Pd^{2+} ions are not coordinated with surface -OH groups at elevated loadings. These observations align well with the results from CO chemisorption, UV-DRS, XPS and TPR.

Catalytic properties for reductive amination of phenol: The catalytic performance of Pd/ZrO_2 catalysts was evaluated for the vapour-phase reductive amination of phenol to aniline (**Scheme-I**). According to previous reports [20-23,41], phenol is initially hydrogenated to cyclohexanone, which subsequently reacts with ammonia to form cyclohexylideneimine as an intermediate. Further hydrogenation produces cyclohexylamine, followed by dehydrogenation to yield aniline. The hydrogenation of phenol to cyclohexanone is considered the rate-determining step in the reaction pathway. Literature reports also suggest that phenol adsorption on the catalyst surface is influenced by the acid–base properties of the support. Adsorption on basic sites favours the formation of cyclohexanone, whereas strong planar adsorption through the hydroxyl group may promote cyclohexanol formation.

In present Pd/ZrO_2 catalyst system, palladium provides metallic active sites for hydrogenation–dehydrogenation reactions, while the basic sites of zirconia facilitate cyclohexanone formation, which is the key intermediate for aniline production. The catalytic results at 523 K are presented in Fig. 7. Phenol conversion increased with Pd loading up to 2 wt.% and decreased at higher loadings. The decline in activity at elevated Pd contents is attributed to the formation of larger Pd crystallites and reduced dispersion. The catalytic activity closely followed the trends observed for CO chemisorption uptake, Pd dispersion, metal surface area and catalyst basicity. The number of basic sites also increased up to 2 wt.% Pd and decreased at higher loadings. These results suggest that phenol conversion is strongly dependent on both the concentration of active Pd sites and the surface basicity of the catalyst. In contrast, aniline selectivity remained nearly constant at approximately 95% for all catalysts irrespective of Pd loading. These observations are consistent with the results obtained from CO chemisorption, UV–DRS, XPS and TPR analyses.

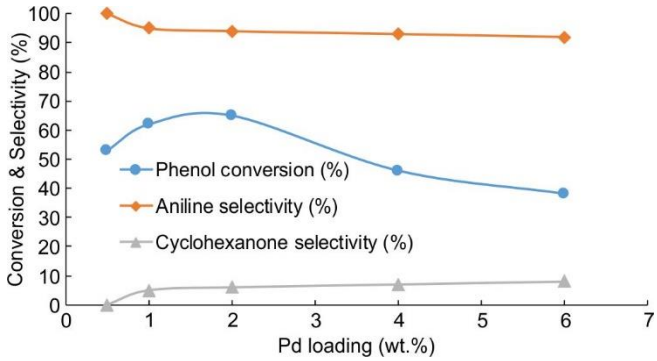

Fig. 7. Reductive amination of phenol over various Pd/ZrO_2 catalysts

The relationship between Pd crystallite size and turnover frequency (TOF) is shown in Fig. 8. The TOF decreased with increasing Pd particle size up to approximately 3 nm and remained nearly constant at larger sizes. Previous studies [21] demonstrated that phenol reductive amination is highly sensitive to Pd dispersion and surface structure. Ortega *et al.* [22] also reported that the coordination environment of Pd significantly influences catalytic activity, confirming the structure-

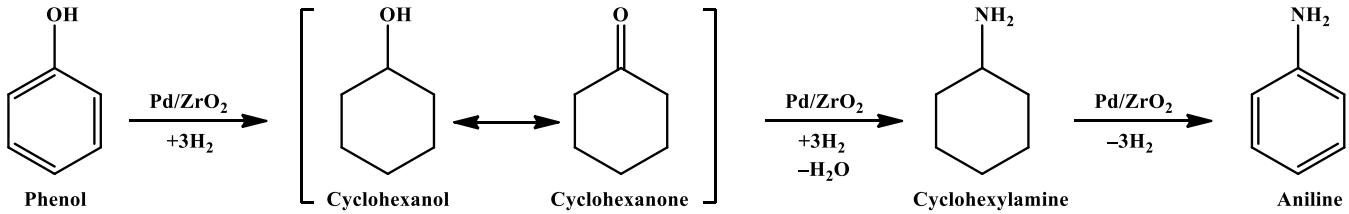

Scheme-I: Reaction pathway of phenol reductive amination to aniline over catalysts (Reactions conditions: Temperature = 523 K; total feed rate = 2.412 (mmol/s); phenol, H_2 and NH_3 mole ratio = 1:5:5; catalyst weight = 0.5 g)

TABLE-6
COMPARISON OF CATALYTIC PROPERTIES OF 2 wt.% OF Pd ON VARIOUS SUPPORTED CATALYSTS

Catalyst	Pd dispersion (%)	Crystallite size (nm)	Conversion (%)	Aniline selectivity (%)	Cyclohexylamine selectivity (%)
2 wt.% Pd/ZrO_2	69.0	1.6	76	95	5
2 wt.% Pd/Al_2O_3	18.3	6.1	37	95	5
2 wt.% Pd/SiO_2	8.9	12.5	10	100	–
2 wt.% Pd/C	23.9	4.7	33	94	6

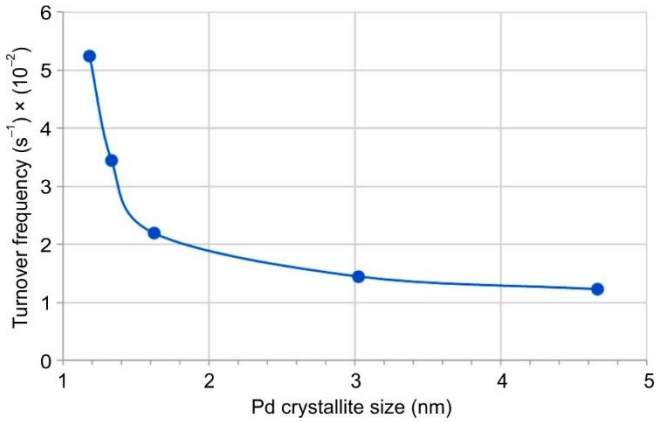

Fig. 8. A correlation between turnover frequency (TOF) *vs*. palladium crystallite size (Pd loading)

sensitive nature of the reaction. The higher TOF observed for smaller Pd particles is attributed to the larger concentration of undercoordinated edge and corner Pd sites, which are considered highly active for phenol reductive amination [42]. These findings indicate that geometric effects and Pd particle structure strongly govern the catalytic behaviour of Pd/ZrO_2 catalysts.

Comparative studies: The catalytic properties of different 2 wt.% Pd-supported catalysts using ZrO_2, Al_2O_3, SiO_2 and activated carbon supports are summarized in Table-6. Among the catalysts investigated, Pd/ZrO_2 exhibited superior phenol conversion and aniline selectivity, which can be attributed to stronger metal–support interaction, higher Pd dispersion and the favourable acid–base characteristics of the zirconia support.

Conclusion

ZrO_2 was identified as an effective support for palladium catalysts in the vapour-phase reductive amination of phenol to aniline due to its ability to stabilize highly dispersed palladium species and provide favourable surface basicity. The XRD analysis confirmed the formation of crystalline PdO only at Pd loadings above 2 wt.%, while lower loadings predominantly contained highly dispersed Pd species. CO chemisorption results demonstrated that Pd dispersion decreased with increasing Pd loading due to particle agglomeration, whereas the number of exposed surface Pd sites increased up to 2 wt.% and remained nearly constant at higher loadings. These observations were in excellent agreement with the UV–Vis DRS, XPS and TPR analyses, which revealed the coexistence of highly dispersed PdO species and bulk PdO crystallites on the ZrO_2 support. The surface basicity of the catalysts also increased up to 2 wt.% Pd and decreased at higher loadings, following a trend similar to catalytic activity. The maximum catalytic performance observed at 2 wt.% Pd strongly correlated with higher Pd dispersion, greater availability of active Pd sites and enhanced catalyst basicity. The catalytic behaviour was therefore governed by the combined influence of Pd–O–Zr electronic interactions, Pd particle size and surface basicity. Furthermore, the strong dependence of activity on Pd crystallite size and coordination environment confirms that the reductive amination of phenol over Pd/ZrO_2 is a structure-sensitive reaction. Among the catalysts investigated, Pd/ZrO_2 exhibited superior catalytic performance and higher dispersion compared with other supported Pd catalysts.

ACKNOWLEDGEMENTS

The authors thank to the Council of Scientific and Industrial Research (CSIR) for the award of a Senior Research Fellowship (SRF).

CONFLICT OF INTEREST

The authors declare that there is no conflict of interests regarding the publication of this article.

DECLARATION OF AI-ASSISTED TECHNOLOGIES

During the preparation of this manuscript, the authors used an AI-assisted tool(s) to improve the language. The authors reviewed and edited the content and take full responsibility for the published work.

REFERENCES

1. C.S. Horbaczewskyi and I.J.S. Fairlamb, *Org. Process Res. Dev.*, **26**, 2240 (2022); https://doi.org/10.1021/acs.oprd.2c00051
2. F. Kong, B. Nie, L. Jiang, X. Luo, R. Lau, D. Zhao, Z. Shao, X. Nie, J. Huang and A. Hassanpouryouzband, *Innov. Mater.*, **3**, 100116 (2025); https://doi.org/10.59717/j.xinn-mater.2024.100116
3. X. Zhao, Y. Chang, W.-J. Chen, Q. Wu, X. Pan, K. Chen and B. Weng, *ACS Omega*, **7**, 17 (2022); https://doi.org/10.1021/acsomega.1c06244
4. A. Rajagopalan, B.A. Thirumalarasu, S. Ramanathan and U.B.R. Ragula, *J. Ind. Eng. Chem.*, (2026); https://doi.org/10.1016/j.jiec.2026.01.057
5. S. Bibi, M. Zubair, R. Riaz, A. Kanwal and S.A.A. Shah, *RSC Adv.*, **15**, 15417 (2025); https://doi.org/10.1039/D5RA01808K
6. Y. Yang, J. Lee, R. Dorakhan, H. Nie, G. Fu, A. Quarantotto, J.Y. Howe and Y.-H.C. Chin, *Appl. Catal. A Gen.*, **629**, 118290 (2022); https://doi.org/10.1016/j.apcata.2021.118290
7. N. Scotti, F. Zaccheria, C. Evangelisti, R. Psaro and N. Ravasio, *Catal. Sci. Technol.*, **7**, 1386 (2017); https://doi.org/10.1039/C6CY02670B
8. R.A. El-Salamony, K. Acharya, A.S. Al-Fatesh, A.I. Osman, S.B. Alreshaidan, N.S. Kumar, H. Ahmed and R. Kumar, *Mol. Catal.*, **547**, 113378 (2023); https://doi.org/10.1016/j.mcat.2023.113378

9. H. Öner Akduman and E. Özdemir, *Int. J. Hydrogen Energy*, **100**, 67 (2025); https://doi.org/10.1016/j.ijhydene.2024.12.261
10. J.R. Sohn, S.G. Cho, Y. Pae and S. Hayashi, *J. Catal.*, **159**, 170 (1996); https://doi.org/10.1006/jcat.1996.0076
11. L.A. Boot, A.J.V. Dillen, J.W. Geus and F.R. Baren, *J. Catal.*, **163**, 195 (1996); https://doi.org/10.1006/jcat.1996.0319
12. K. Chen, Y. Fan, Z. Hu and Q. Yan, *Catal. Lett.*, **36**, 139 (1996); https://doi.org/10.1007/BF00807610
13. H. Inokawa, S.F. Zaman, H. Driss, M. Daous, A. Al-Zahrani, H. Miyaoka, T. Ichikawa, Y. Kojima and L.A. Petrov, *IOP Conf. Series Mater. Sci. Eng.*, **458**, 012018 (2018); https://doi.org/10.1088/1757-899X/458/1/012018
14. W.J. Shen, M. Okumura, Y. Matsumura and M. Haruta, *Appl. Catal. A Gen.*, **213**, 225 (2001); https://doi.org/10.1016/S0926-860X(01)00465-3
15. N. Iwasa, O. Yamamoto, T. Akazawa, S. Ohyama and N. Takezawa, *J. Chem. Soc. Chem. Commun.*, **1322-1323**, 1322 (1991); https://doi.org/10.1039/c39910001322
16. K. Okumura, T. Kobayashi, H. Tanaka and M. Niwa, *Appl. Catal. B*, **44**, 325 (2003); https://doi.org/10.1016/S0926-3373(03)00101-2
17. A. Mary, N. Kanagathara and A.R.B. Suganthi, *Mater. Today Proc.*, **33**, 4751 (2020); https://doi.org/10.1016/j.matpr.2020.08.358
18. E.Y. Bezuglaya, A.B. Shchutskaya and I.V. Smirnova, *Atmos. Environ., A Gen. Topics*, **27**, 773 (1993); https://doi.org/10.1016/0960-1686(93)90195-5
19. S.K. Ong and A.R. Bowers, *J. Environ. Eng.*, **116**, 1013 (1990); https://doi.org/10.1061/(ASCE)0733-9372(1990)116:6(1013).
20. Y. Ono, *J. Catal.*, **72**, 121 (1981); https://doi.org/10.1016/0021-9517(81)90083-X
21. D. Naresh, V.P. Kumar, M. Harisekhar, N. Nagaraju, B. Putrakumar and K.V.R. Chary, *Appl. Surf. Sci.*, **314**, 199 (2014); https://doi.org/10.1016/j.apsusc.2014.06.156
22. M. Ortega, D. Gómez, R. Manrique, G. Reyes, J.T. García-Sánchez, V.G. Baldovino Medrano, R. Jiménez and L.E. Arteaga-Pérez, *React. Chem. Eng.*, **8**, 47 (2023); https://doi.org/10.1039/D2RE00259K
23. T. Cuypers, T. Morias, S. Windels, C. Marquez, C. Van Goethem, I. Vankelecom and D.E. De Vos, *Green Chem.*, **22**, 1884 (2020); https://doi.org/10.1039/C9GC02625H
24. S. Velu, M.P. Kapoor, S. Inagaki and K. Suzuki, *Appl. Catal. A Gen.*, **245**, 317 (2003); https://doi.org/10.1016/S0926-860X(02)00655-5
25. L.M. Sikhwivhilu, N.J. Coville, D. Naresh, K.V.R. Chary and V. Vishwanathan, *Appl. Catal. A Gen.*, **324**, 52 (2007); https://doi.org/10.1016/j.apcata.2007.03.004
26. K.V.R. Chary, D. Naresh, V. Vishwanathan, M. Sadakane and W. Ueda, *Catal. Commun.*, **8**, 471 (2007); https://doi.org/10.1016/j.catcom.2006.07.017
27. A.Yu. Stakheev, D.A. Bokarev, I.P. Prosvirin and V.I. Bukhtiyarov, in eds.: V.A. Sadykov, Particle-Size Effect in Catalytic Oxidation Over Pt Nanoparticles: Advanced Nanomaterials for Catalysis and Energy Synthesis, Characterization and Applications Advanced Nanomaterials, Chap. 8, pp 295-320 (2019); https://doi.org/10.1016/B978-0-12-814807-5.00008-5
28. J.M.D. Cónsul, C.A. Peralta, E.V. Benvenutti, J.A.C. Ruiz, H.O. Pastore and I.M. Baibich, *J. Mol. Catal. Chem.*, **246**, 33 (2006); https://doi.org/10.1016/j.molcata.2005.10.011
29. E.H. Voogt, A.J.M. Mens, O.L.J. Gijzeman and J.W. Geus, *Surf. Sci.*, **350**, 21 (1996); https://doi.org/10.1016/0039-6028(96)01028-X
30. M.P. Kapoor, Y. Ichihashi, W.-J. Shen and Y. Matsumura, *Catal. Lett.*, **76**, 139 (2001); https://doi.org/10.1023/A:1012249529720
31. Y. Takasu, R. Unwin, B. Tesche, A.M. Bradshaw and M. Grunze, *Surf. Sci.*, **77**, 219 (1978); https://doi.org/10.1016/0039-6028(78)90003-1
32. T. Fleisch, *J. Catal.*, **87**, 398 (1984); https://doi.org/10.1016/0021-9517(84)90200-8
33. N.S. Babu, N. Lingaiah, R. Gopinath, P.S. Sankar Reddy and P.S. Sai Prasad, *J. Phys. Chem. C Nanomater. Interfaces*, **111**, 6447 (2007); https://doi.org/10.1021/jp065866r
34. D. Luo, Z. Tang, X. Yu, T. Zhang, C.-R. Chang and Z. Hu, *Appl. Catal. B*, **339**, 123117 (2023); https://doi.org/10.1016/j.apcatb.2023.123117
35. G. Liu, S. Liu, S. Liu, S. Yu, L. Li, F. Liu, C. Xie and X. Song, *Catal. Lett.*, **147**, 987 (2017); https://doi.org/10.1007/s10562-016-1940-1
36. M.L. Cubeiro and J.L.G. Fierro, *Appl. Catal. A Gen.*, **168**, 307 (1998); https://doi.org/10.1016/S0926-860X(97)00361-X
37. S.F. Parker, H.C. Walker, S.K. Callear, E. Grünewald, T. Petzold, D. Wolf, K. Möbus, J. Adam, S.D. Wieland, M. Jiménez-Ruiz and P.W. Albers, *Chem. Sci.*, **10**, 480 (2019); https://doi.org/10.1039/C8SC03766C
38. L.M. Esteves, M.H. Brijaldo and F.B. Passos, *J. Mol. Catal. Chem.*, **422**, 275 (2016); https://doi.org/10.1016/j.molcata.2016.02.001
39. R.V. Mikhaylov, K.V. Nikitin, N.I. Glazkova and V.N. Kuznetsov, *J. Photochem. Photobiol. Chem.*, **360**, 255 (2018); https://doi.org/10.1016/j.jphotochem.2018.04.055
40. K.V.R. Chary, G.V. Sagar, C.S. Srikanth and V.V. Rao, *J. Phys. Chem. B*, **111**, 543 (2007); https://doi.org/10.1021/jp063335x
41. R. Jiang, Z. Xie, C. Zhang and Q. Chen, *Catal. Today*, **93-95**, 359 (2004); https://doi.org/10.1016/j.cattod.2004.06.024
42. O.E. Brandt Corstius, J.E.S. van der Hoeven, G.J. Sunley and P.E. de Jongh, *J. Catal.*, **427**, 115103 (2023); https://doi.org/10.1016/j.jcat.2023.115103